SUPPLEMENTARY INFORMATION:
Hybrid ferroelectric-ionic memristive in-memory computing platform

Wonjun Shin,[1,2†*] Jeong-Han Kim,[3†] Ryun-Han Koo,[4†] Jangsaeng Kim,[1,5†] Eugene Park,[6†] Piush Behera,[1] Sojin Kim,[7] Jinseok Hong,[7] Feras Al Dirini,[1] Been Kwak,[3] Jiwon You,[3] Jiseong Im,[4] Dooyong Koh,[1,8] Yejin Hong,[1,8] Qinyuan Xue,[1,8] Hyunho Seok[1], Youngchan Cho,[2] Hwiin Ju,[9] Wooje Jung,[9] Kyunghwan Lee,[9] Daewon Ha,[9] Jong-Ho Lee,[4] Seung-Yong Lee,[7,10] Deok-Hwang Kwon,[11] Frances M. Ross,[6] Youngho Kang,[12] Suraj S. Cheema,[1,6,8*] Daewoong Kwon[3*]

[1]*Research Laboratory of Electronics, Massachusetts Institute of Technology, Cambridge, MA, USA.*

[2]*Department of Semiconductor Convergence Engineering, Sungkyunkwan University, Suwon, Republic of Korea*

[3]*Department of Electronic Engineering, Hanyang University, Seoul, Republic of Korea*

[4]*Department of Electrical and Computer Engineering and Inter-university Semiconductor Research Center, Seoul National University, Seoul, Republic of Korea*

[5]*Department of System Semiconductor Engineering, Sogang University, Seoul 04107, South Korea*

[6]*Department of Materials Science and Engineering, Massachusetts Institute of Technology, Cambridge 02139, MA, USA*

[7]*Division of Materials Science and Engineering, Hanyang University, Seoul, Republic of Korea*

[8]*Department of Electrical Engineering and Computer Science, Massachusetts Institute of Technology, Cambridge, MA, USA.*

[9]*Advanced Device Research Laboratory, Semiconductor Research Center, Samsung Electronics Co., Ltd, South Korea*

[10]*Department of Battery Engineering, Hanyang University, Seoul 04763, Republic of Korea*

[11]*Energy Materials Research Center, Korea Institute of Science and Technology, Seoul 02792, Republic of Korea*

[12]*Department of Materials Science and Engineering, Incheon National University, Incheon 22012, Korea*

[†] *These authors contributed equally: Wonjun Shin, Jeong-Han Kim, Ryun-Han Koo, Jangsaeng Kim, Eugene Park*

[*] *Correspondence to: swj0107@mit.edu (W.S), sscheema@mit.edu (S.S.C); dw79kwon@hanyang.ac.kr (D.K)*

Table of Contents

Supplementary Table 1. | Previous study on HfO_2-based tunnel junctions with ionic oxygen vacancy migration-based switching mechanism. These studies predominantly relied on the formation and rupture of conductive filaments associated with oxygen vacancies.

Device structure	Electrode area	On/off ratio	CMOS compatibility	Ref.
TiN/IL/HfO_2/Pt Pt/HfO_2/Pt	Not shown	< 1000	Pairtially yes (Pt)	**1**
TiN/HfO_x/TiN	2500 μm^2	< 100	No	**2**
TiN/V/HfO_2/Pt	0.36 μm^2	10^3	Pairtially yes (Pt)	**3**
Pt/HfO_2/TiN	31400 μm^2	< 1000	Pairtially yes (Pt)	**4**
Pt/HfO_2/Ti	10000 μm^2	19.2	Pairtially yes (Pt)	**5**
ITO/TiO_2/HfO_2/Pt	7850 μm^2	< 200	Pairtially yes (Pt)	**6**
Pt/HfO_2/Ag/Pt	100 μm^2	10^8	Pairtially yes (Pt)	**7**
Pt/HfO_2/Pt	9 μm^2	10^6	Pairtially yes (Pt)	**8**
Pt/Al:HfO_2/TiN	10000 μm^2	1900	Pairtially yes (Pt)	**9**
Nb/NbO_x/Al_2O_3/HfO_2/Au	625 μm^2	< 1000	No	**10**

Supplementary Table 2. | Previous study on HfO_2-based tunnel junctions with ferroelectric polarization switching mechanism. While the majority of these studies demonstrated considerably lower on/off ratios compared to the HTD examined in this study, one notable exception was a tunnel junction employing Pt/HZO/Nb:STO[22], which exhibited a on/off ratio of 2×10^7. However, the inclusion of Nb:STO as the top electrode in this configuration renders it incompatible with CMOS fabrication processes. Moreover, due to the MFM structure, the rectifying ratio of the device[22] is only 5 which cannot be integrated into large-size arrays without rectifying FETs.

Device structure	Electrode area	On/off ratio	Rectifying ratio	Ferroelectric film thickness	Structure	CMOS compatibility	Ref.
Au/Co/BTO/LSMO	0.25 μm^2	100	1.5	2 nm	MFIS	No	[11]
Pt/HZO/TiN	70650 μm^2	15	1	6 nm	MFM	Yes	[12]
TiN/HZO/Ge	3847 μm^2	30	1.2	6 nm	MFIS	Yes	[13]
TiN/HZO/Ge	3847 μm^2	7	1.4	8 nm	MFIS	Yes	[13]
TiN/HZO/Ge	3847 μm^2	1	1.3	10 nm	MFIS	Yes	[13]
Ni/HZO/IL/TiN	Not shown	132	52	9 nm	MFIM	Yes	[14]
TiN/HZO/SiO_2/p-Si	100 μm^2	9	N/A	4 nm	MFIS	Yes	[15]
Ag/$BaTiO_3$/Nb:$SrTiO_3$	9 μm^2	10	1	2.4 nm	MFM	No	[16]
Pt/STO/HZO/LSMO/STO	314 μm^2	1.13	Not shown	4.6 nm	MFIM	No	[17]
TiN/HZO/Al_2O_3(1.0 nm)/p-Ge	100 × 100 μm^2	19	1.1	8.4 nm	MFIS	Yes	[18]
TiN/HZO/Al_2O_3(1.8 nm)/p-Ge	100 × 100 μm^2	11	1.1	8.4 nm	MFIS	Yes	[18]
TiN/HZO/Al_2O_3(2.2 nm)/p-Ge	100 × 100 μm^2	4	1.2	8.4 nm	MFIS	Yes	[18]
W/$Hf_{0.8}Zr_{0.2}O_2$/SiO_2/Si	Not shown	200	1	1 nm	MFIS	Yes	[19]
TiN/HZO/Al_2O_3/Ni	1 μm^2	4	1.2	5 nm	MFIM	Yes	[20]
TiN/HZO/Al_2O_3/Ni	1 μm^2	12	1.4	6 nm	MFIM	Yes	[20]
TiN/HZO/Al_2O_3/Ni	1 μm^2	50	1.3	7 nm	MFIM	Yes	[20]
TiN/HZO/Al_2O_3/Ni	1 μm^2	90	1.2	9 nm	MFIM	Yes	[20]
Au/HZO/LSMO/Nb:STO	31400 μm^2	834	4	4.3 nm	MFIS	No	[21]
Pt/HZO/Nb:STO	100 μm^2	2×10^7	5.1	1.5 nm	MFIS	No	[22]
TiN/$HfAlO_x$/SiO_2/n^+-Si	100 × 100 μm^2	29	22	9 nm	MFIS	Yes	[23]
TiN/$HfAlO_x$/HfO_2/n^+-Si	100 × 100 μm^2	57	21	9 nm	MFIS	Yes	[23]
TiN/$HfAlO_x$/ZrO_2/n^+-Si	100 × 100 μm^2	21	7	9 nm	MFIS	Yes	[23]
Mo/HfO_2/HZO/SiO_2/n^+-Si	100 × 100 μm^2	263	402	10 nm	MFIS	Yes	[24]
Mo/HZO/HfO_2/SiO_2/n^+-Si	100 × 100 μm^2	234	204	10 nm	MFIS	Yes	[24]
TiN/HZO/SiO_2/n^+-Si	100 × 100 μm^2	12	20.7	12 nm	MFIS	Yes	[25]
TiAl/HZO/SiO_2/n^+-Si	100 × 100 μm^2	30	15.5	12 nm	MFIS	Yes	[25]
TiN/HZO/W	Not shown	7	1.2	5.5 nm	MFIM	Yes	[26]
TiN/HZO/TaN/W	Not shown	50	110	5.5 nm	MFIM	Yes	[26]
W/TaO/HZO/W	Not shown	150	1500	5.5 nm	MFIM	Yes	[27]
Mo/HZO/Al_2O_3/Ti/Mo	100 × 100 μm^2	59	35.7	6 nm	MFIM	Yes	**This work**

Supplementary Table 3. | Previous study on HfO_2-based tunnel junctions with both ferroelectric-ionic switching mechanisms. Since 2018, the mixture of switching mechanisms of ferroelectric-ionic has been reported, they focused on revealing the co-existence of these switching mechanisms[28–30,33,34]. Investigations into the synergistic switching behavior have only recently emerged[31,32]. However, the origin of this synergy remains elusive. We reveal that the potential barrier for the ferroelectric polarization can be lowered by charged oxygen vacancies.

Device structure	Electrode area	On/off ratio	Rectifying ratio	Ferroelectric film thickness	Structure	CMOS compatibility	Note	Ref.
TiN/Sr:HfO_2/Pt	3100 μm^2	Ionic (1.17×10^3) FE (Not shown)	1.2	5 nm	MFM	Yes	Seperate switching between ionic and FE	[28]
LSMO/HZO/Pt	628 μm^2	Ionic (7.13×10^1) FE (4.14)	1.8	4.6 nm	MFS	No	Seperate switching between ionic and FE	[29]
TiN/HZO/SiO_2/p^+-Si	15700 μm^2	Ionic (7.23×10^1) FE (2.21)	24	4.5 nm	MFIS	Yes	Seperate switching between ionic and FE	[30]
LSMO/HZO/LSMO	Not shown	Not shown	Not shown	6 nm	MFM	No	Intertwined switching between ionic and FE	[31]
Si/HZO/not shown	Not shown	Not shown	Not shown	10 nm	-	N/A	Intertwined switching between ionic and FE	[32]
TiN/HfO_2/SiO_2/n^+-Si	100×100 μm^2	Ionic (1.12×10^1) FE (2.57×10^2)	152	6 nm	MFIS	Yes	Seperate switching between ionic and FE	[33]
TiN/HfO_2/SiO_2/p^+-Si	100×100 μm^2	4.23×10^2	950	9 nm	MFIS	Yes	Seperate switching between ionic and FE	[34]
TiN/HfO_2/SiO_2/n^+-Si	100×100 μm^2	2.41×10^2	150	9 nm	MFIS	Yes	Seperate switching between ionic and FE	[34]
Mo/HZO/Al_2O_3/Ti/Mo	100×100 μm^2	HTD (1.2×10^5)	3.29×10^6	6 nm	MFIM	Yes	Synergistic switching in single HTD	**This work**

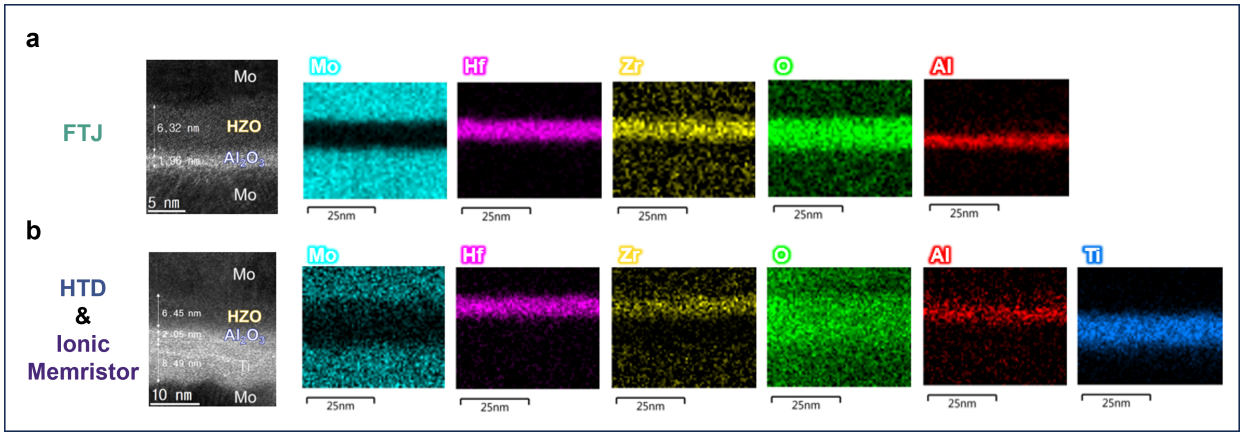

Supplementary Fig. 1. | Cross-sectional TEM analysis of tunnel junctions. (a, b) Cross-sectional TEM images and EDS elemental analyses of FTJ (a) and HTD/ionic memristor (b). This confirms the thickness and the spatial distribution of each element throughout of tunnel junctions.

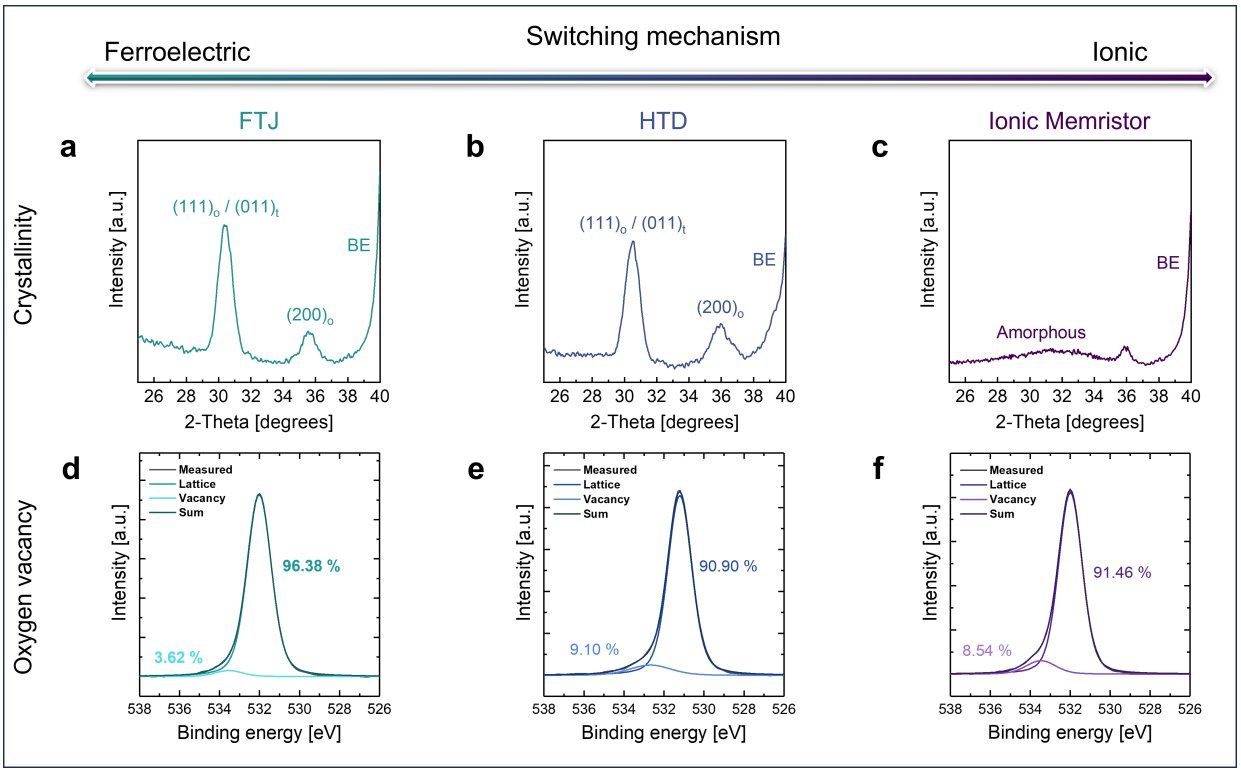

Supplementary Fig. 2. | XRD and XPS analysis of tunnel junctions. (a,b,c) GIXRD analysis of the FTJ (a), HTD (b), and ionic memristor (c). Both the FTJ and HTD present a peak at approximately $2\theta = 30.5°$, whereas the ionic memristor exhibits an amorphous state. **(d,e,f)** XPS analysis of the FTJ (d), HTD (e), and ionic memristor (f). Oxygen vacancy ratios were extracted by deconvoluting O_{1s} spectra into two distinct peaks corresponding to lattice oxygen and oxygen vacancy.

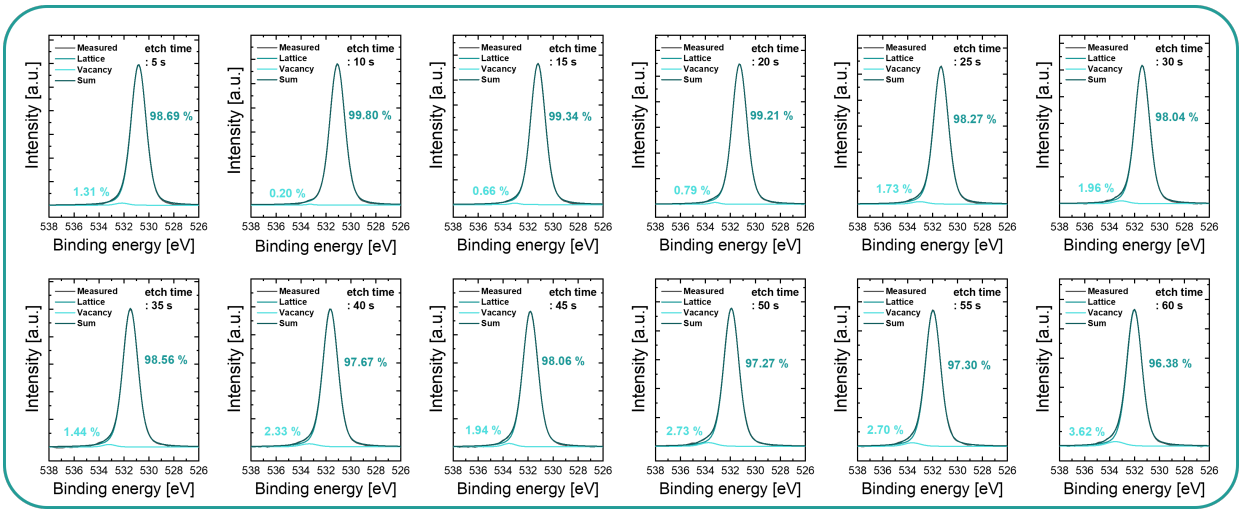

Supplementary Fig. 3. | Deconvoluted O_{1s} spectra of FTJ in XPS analysis. Oxygen vacancy ratios of FTJ were extracted by deconvoluting O_{1s} spectra into two distinct peaks corresponding to lattice oxygen and oxygen vacancy according to the etch time from 5 s (near the TE) to 60 s (near the BE). XPS analysis was performed after removing the top electrode by wet etching, and O_{1s} spectra were deconvoluted after calibrating the peak of C_{1s} spectra at 284.8 eV. The extracted oxygen vacancy ratios were 1.31, 0.20, 0.66, 0.79, 1.73, 1.96, 1.44, 2.33, 1.94, 2.73, 2.70, and 3.62 %, indicating that the trend of oxygen vacancy ratios increases toward the interface between the ferroelectric layer and the interlayer.

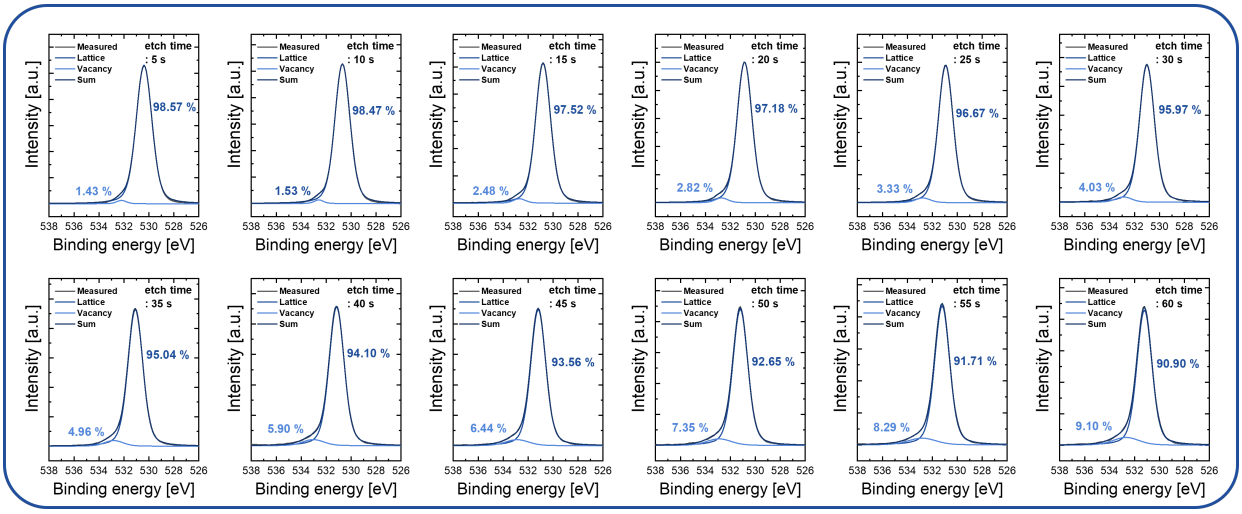

Supplementary Fig. 4. | Deconvoluted O_{1s} spectra of HTD in XPS analysis. Oxygen vacancy ratios of HTD were extracted by deconvoluting O_{1s} spectra into two distinct peaks corresponding to lattice oxygen and oxygen vacancy according to the etch time from 5 s (near the TE) to 60 s (near the BE). XPS analysis was performed after removing the top electrode by wet etching, and O_{1s} spectra were deconvoluted after calibrating the peak of C_{1s} spectra at 284.8 eV. The extracted oxygen vacancy ratios were 1.43, 1.53, 2.48, 2.82, 3.33, 4.03, 4.96, 5.90, 6.44, 7.35, 8.29, and 9.10 % indicating that the trend of oxygen vacancy ratios increases toward the interface between the ferroelectric layer and the interlayer like FTJ, but the oxygen vacancy ratio is almost twice of FTJ.

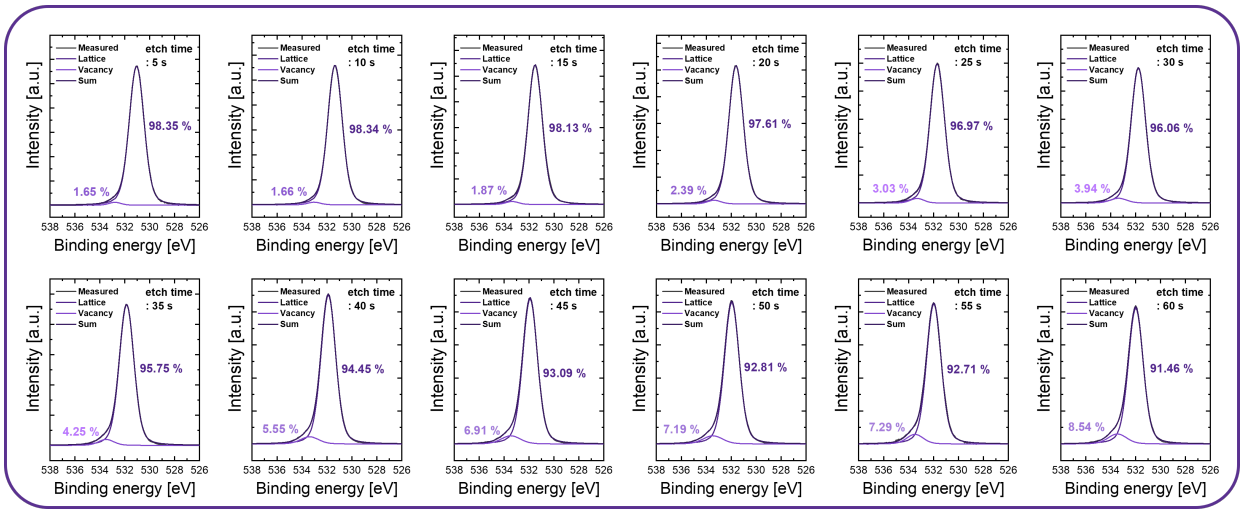

Supplementary Fig. 5. | Deconvoluted O_{1s} spectra of ionic memristor in XPS analysis. Oxygen vacancy ratios of ionic memristor were extracted by deconvoluting O_{1s} spectra into two distinct peaks corresponding to lattice oxygen and oxygen vacancy according to the etch time from 5 s (near the TE) to 60 s (near the BE). XPS analysis was performed after removing the top electrode by wet etching, and O_{1s} spectra were deconvoluted after calibrating the peak of C_{1s} spectra at 284.8 eV. The extracted oxygen vacancy ratios were 1.65, 1.66, 1.87, 2.39, 3.03, 3.94, 4.25, 5.55, 6.91, 7.19, 7.29, and 8.54 % indicating that the oxygen vacancy ratio is similar to HTD, which is almost twice of FTJ.

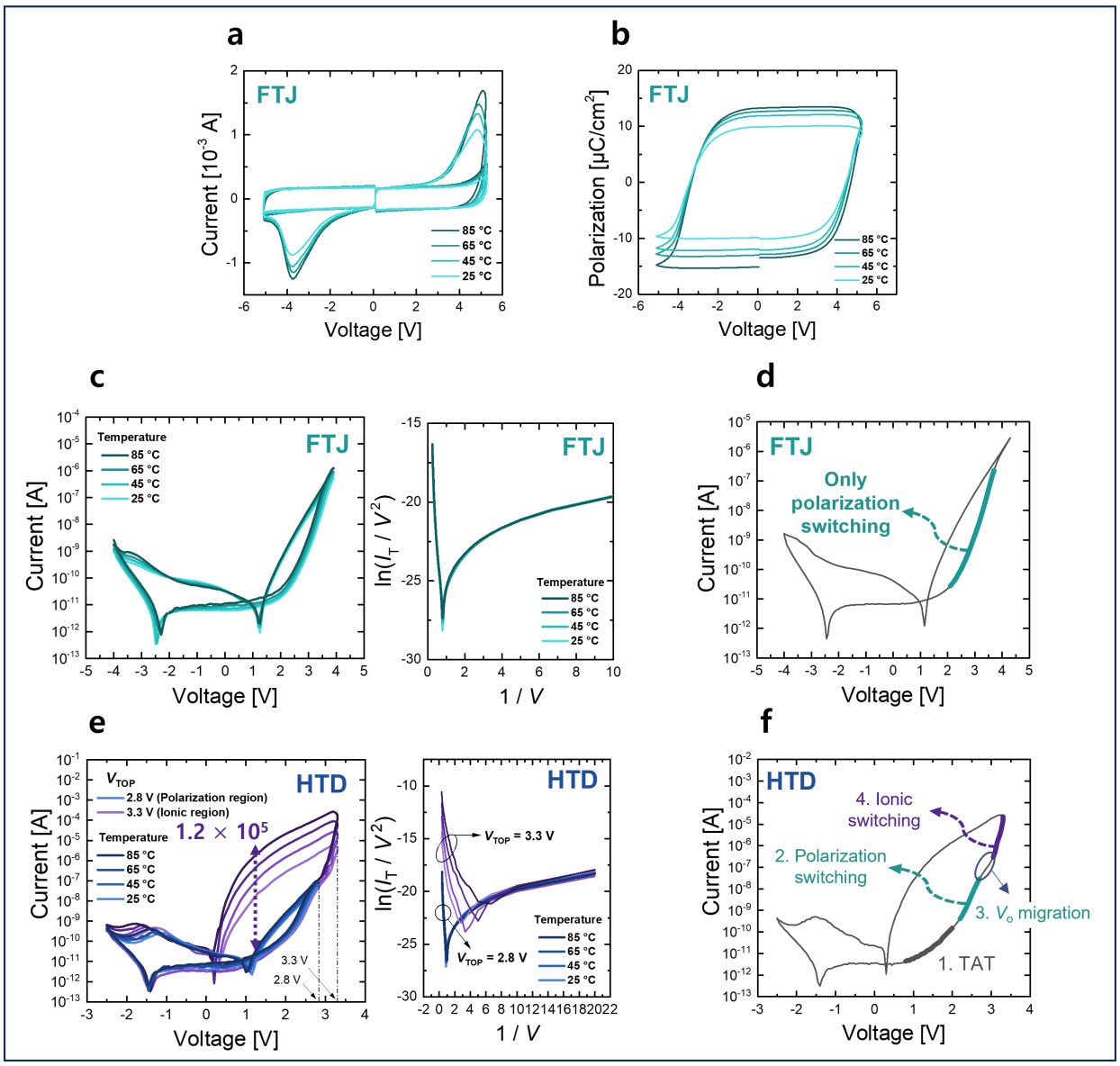

Supplementary Fig. 6. | Electrical characteristics according to various temperatures. (a,b) Polarization of FTJ according to temperature was measured by PUND method (a) and the $P-V$ curves (b) were extracted from measured PUND measurements. **(c)** The hysteretic tunneling current (I_T) of FTJ was measured with various temperatures and the corresponding F-N plot (ln (I_T/V^2) - 1/V) was plotted. I_T of FTJ didn't increase despite the increase in temperature and F-N plot is linear in the low 1/V region (high voltage region), which shows that F-N tunneling by polarization switching is dominant in FTJ. **(d)** The region of polarization switching in the I_T-V curve of FTJ. **(e)** I_T of HTD according to temperature was measured with two V_{TOP}s in order to separate the region with the resistive switching (V_{TOP} = 3.3 V) from the region with

only polarization switching(V_{TOP} = 2.8 V), and the corresponding F-N plot was plotted. When measured at a V_{TOP} of 2.8 V, the trend of I_T and F-N plots of HTD are similar to FTJ. However, $I_T$of HTD increases with increasing temperature and F-N plot is not linear when measured at a V_{TOP} of 3.3 V. Because HTD has a lot of oxygen vacancies in the HZO layer due to the oxygen scavenging layer, and 3.3 V can move the oxygen vacancies in the HZO layer to the interface between the HZO layer and the interlayer, whereas 2.8 V is not enough to move the oxygen vacancies to the interface. **(f)** The region of polarization switching and resistive switching in the I_T-V curve of HTD. In low positive voltage regions, I_T of HTD increases early and gradually due to trap-assisted tunneling (TAT) because HTD has a lot of oxygen vacancies in the HZO layer, and oxygen vacancy can act as the site of TAT.

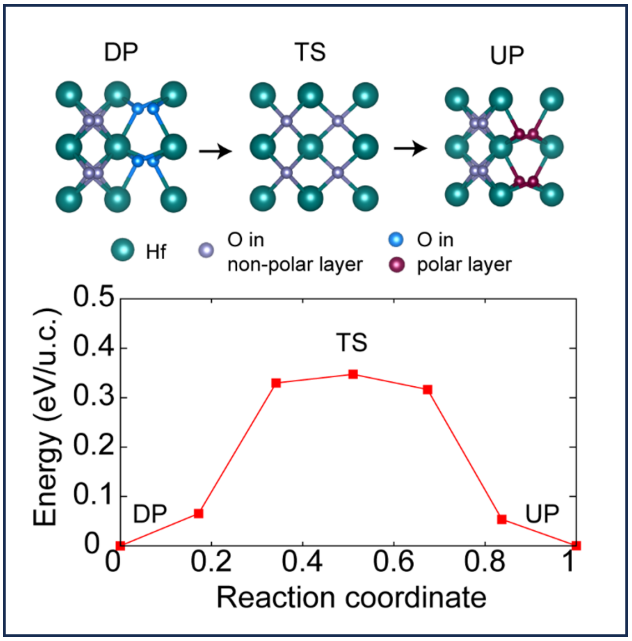

Supplementary Fig. 7. | Energy profile for uniform polarization switching in o-HfO_2. DP, TS, and UP denote downward polarization, transition state, and upward polarization, respectively. During polarization switching, the tetragonal-like atomic arrangement occurs, forming the transition state.

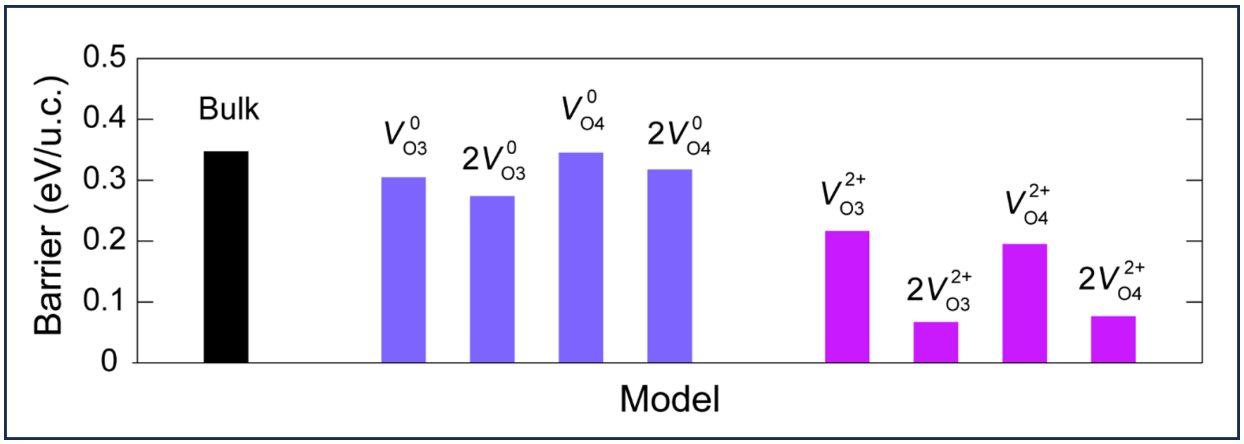

Supplementary Fig. 8. | Uniform polarization switching dynamics depending on V_{OS}. Energy barriers for uniform polarization switching in bulk with and without oxygen vacancies.

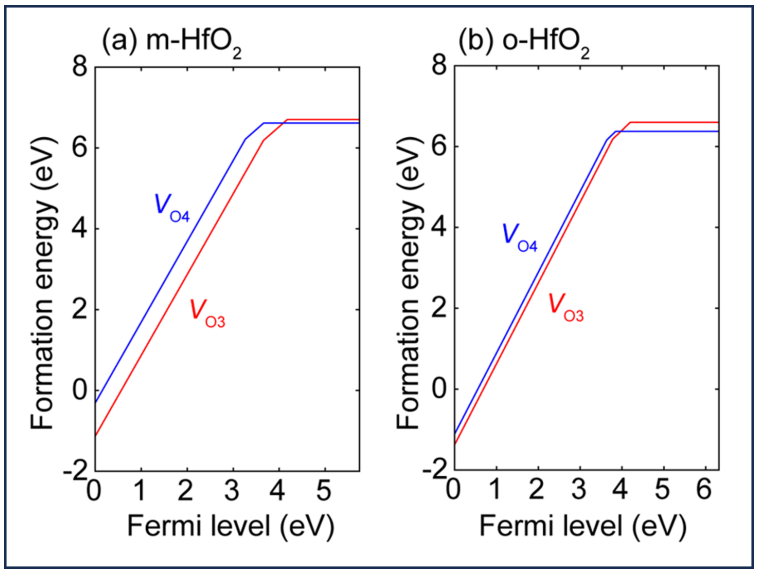

Supplementary Fig. 9. | Oxygen vacancy formation energy. (a,b) Oxygen-vacancy formation energies in monoclinic (a) and orthorhombic (b) HfO_2. V_{O3} and V_{O4} indicate oxygen vacancies that are created by removing an oxygen atom with three- and four- fold coordination, respectively. The slope of the formation-energy curve indicates the charge state.

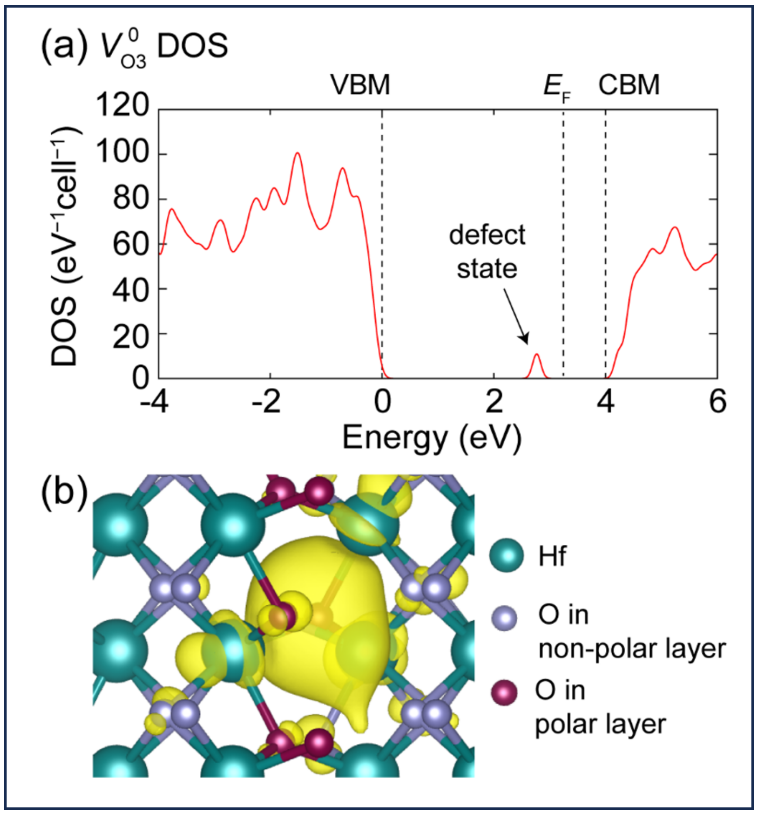

Supplementary Fig. 10. | Density of states. (a) Density of states of bulk with an oxygen vacancy in the neutral state (V_{O3}^{0}). **(b)** Partial charge density distribution of the defect state in (a). In the neutral state, two electrons occupy the defect state localized near the vacancy site, whereas they are removed in the doubly positively charged state (V_{O3}^{2+}). V_{O4} also shows a similar electronic structure.

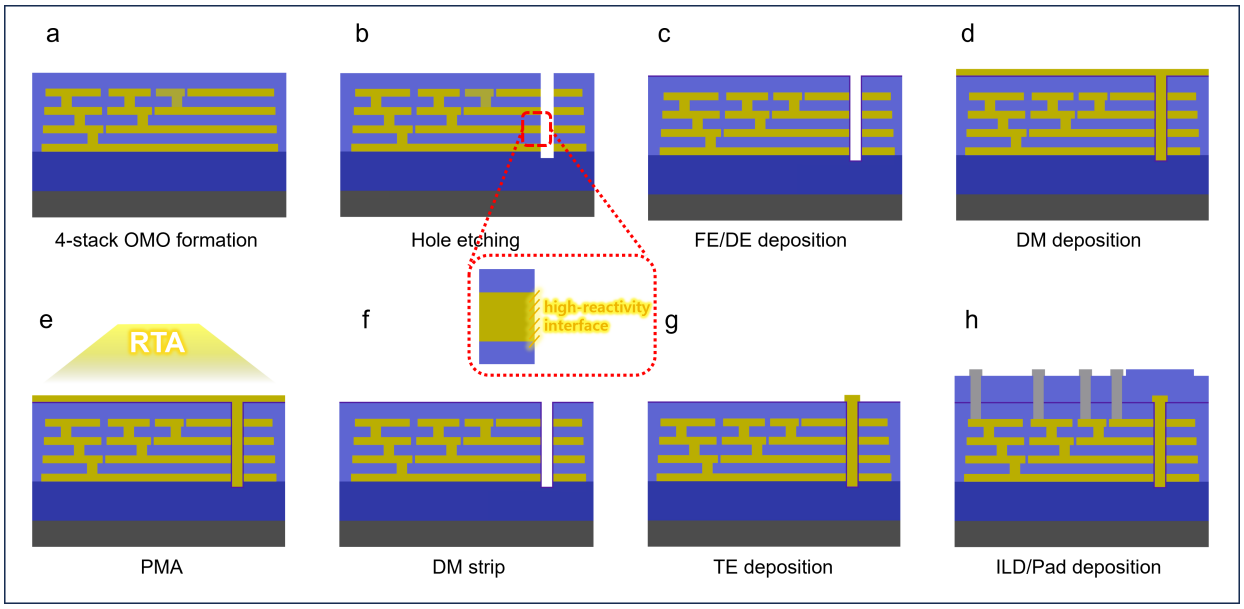

Supplementary Fig. 11. | Fabrication process of 3D HTD. The 4-stack 3D HTD was fabricated on p-type silicon substrates. **(a)** 4-stack oxide-metal-oxide structure (OMO) formation. **(b)** Hole-pattern etching. The etched surface of TiN become more reactive, which can perform the role of oxygen scavenging layer. **(c)** Dielectric and ferroelectric layers deposition. Al_2O_3 layer is formed with trimethyl aluminum (TMA) precursor as dielectric and HZO layer is formed using tetrakis (ethylmethylamino) hafnium (TEMAHf) and tetrakis (ethylmethylamino) zirconium (TEMAZr) precursors as ferroelectric layer. These films were sequentially conducted using thermal ALD (CN-1). **(d)** TiN was deposited as the dummy metal using thermal ALD (CN-1) for good step coverage. **(e)** PMA for inducing ferroelectricity. The PMA was performed at 500 °C. **(f)** Dummy metal removal using SC-1 solution. **(g)** TiN formation using thermal ALD as the top electrode. **(h)** ILD deposition and pad metal formation.

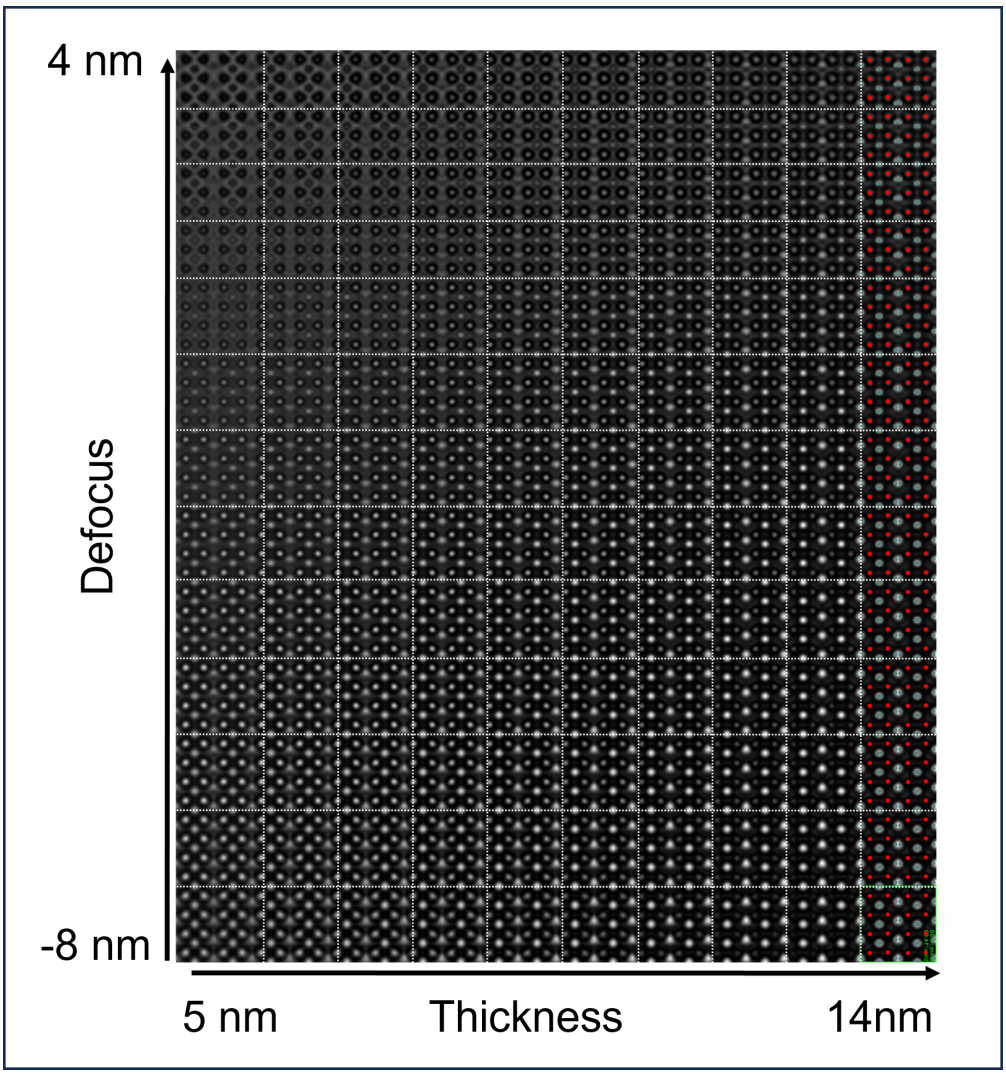

Supplementary Fig. 12. | Simulated Atomic Resolution Images Using Bloch Method. Atomic resolution HR-TEM images of the orthorhombic Hf-Zr-O phase (space group 29, $Pbc2_1$) are simulated under varying defocus and sample thickness, using a spherical aberration (Cs) value of -15 μm. The simulated images at a thickness of approximately 10 nm and slightly under-focused conditions show a good match with the experimental data. Displaced oxygen sites (II), which deviate from centrosymmetry, are clearly visible. Oxygen sites are highlighted in grey, while Hf-Zr sites are marked in red in the right-hand column.

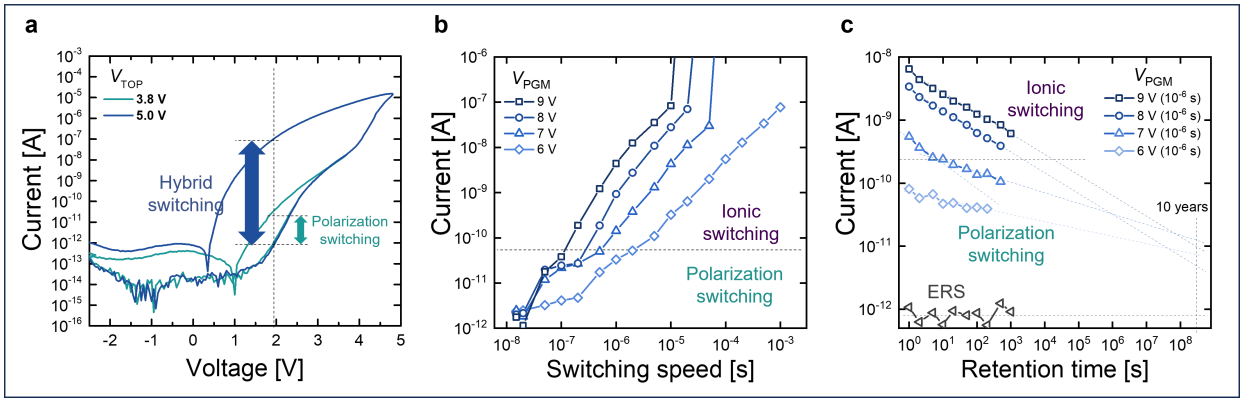

Supplementary Fig. 13. | DC and pulsed program characteristics of 3D HTD. (a) Tunneling current versus voltage curves of 3D HTD, demonstrating the coexistence of polarization and ionic switching mechanisms. The polarization switching is dominant when the bias applied to the top electrode is small (V_{TOP} = 3.8 V). The ionic switching introduces additional enhancement in the on/off ratio by hybrid switching when a large voltage is applied to the top electrode (V_{TOP} = 5.0 V). **(b)** Pulsed operation-based switching behaviors of HTD. The 3D HTD shows a unique switching behavior with distinct slopes observed depending on the switching mechanism. **(c)** Retention characteristics of 3D HTD. Different switching behaviors lead to distinct retention characteristics with varying slopes over time depending on the type of switching.

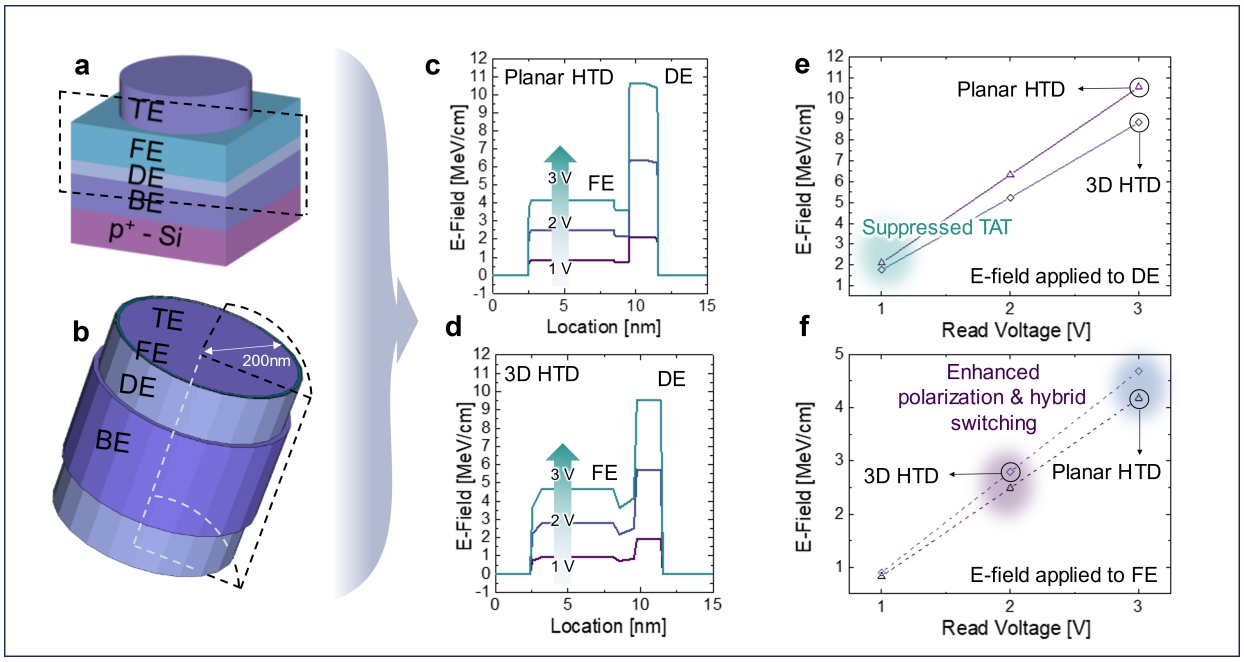

Supplementary Fig. 14. | TCAD simulation of the field distribution in 3D HTD. (a,b) Schematic of the planar HTD (a) and 3D HTD (b). **(c,d)** Energy band diagram of the planar HTD (c) and 3D HTD (d) with the increase in the program bias. **(e,f)** Electric field distribution in the DE (e) and FE (f) in the planar HTD and 3D HTD.

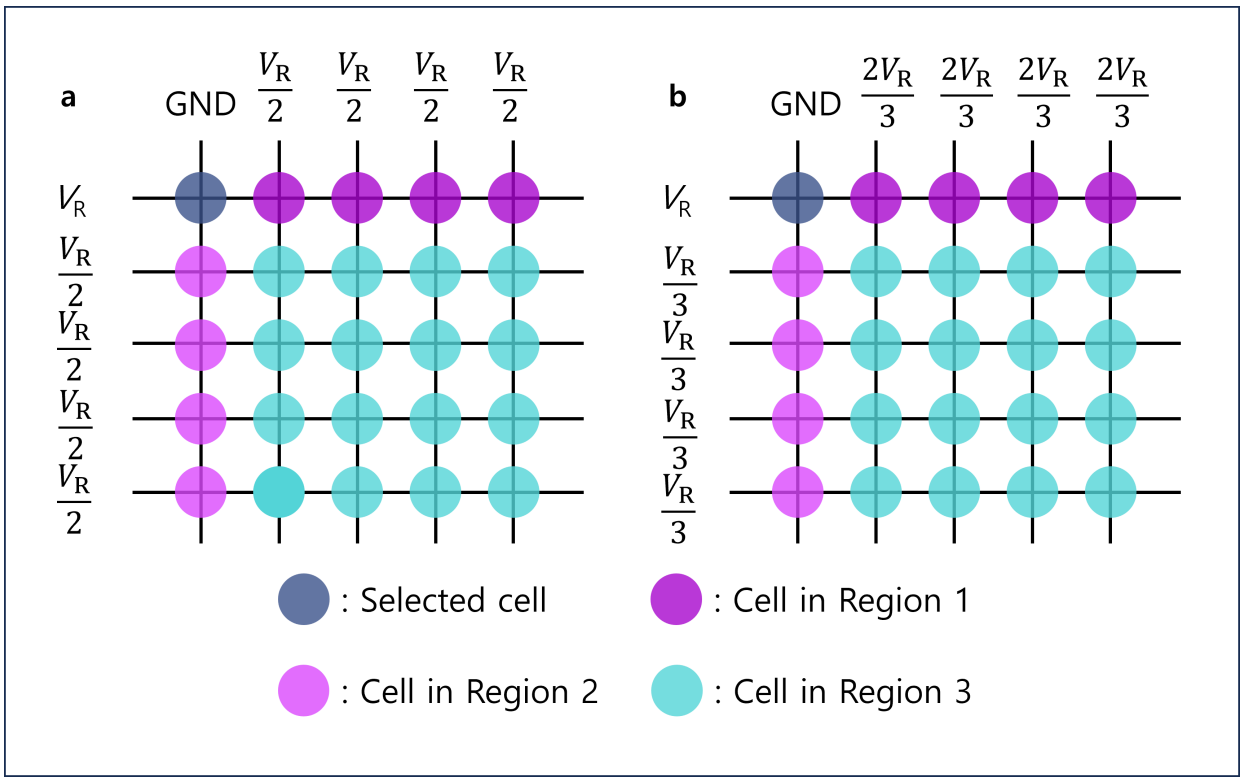

Supplementary Fig. 15. | Read schemes in crossbar array with two-terminal tunnel junctions. (a) $V_R/2$ scheme: $V_R/2$ voltage is applied to all unselected lines. **(b)** $V_R/3$ scheme: $V_R/3$ voltage is applied to unselected word lines, while $2V_R/3$ voltage is applied to unselected bit lines. In all read schemes, V_R is applied to the selected word line, and the selected bit line is grounded.

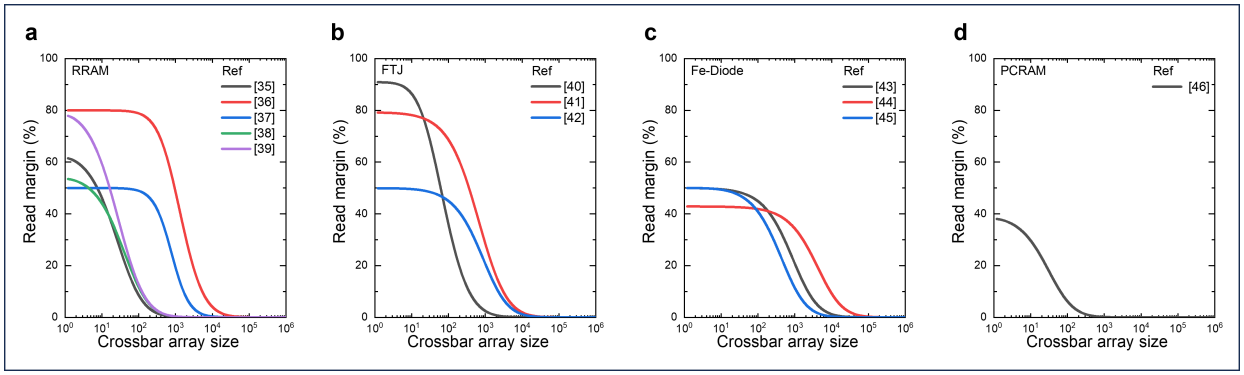

Supplementary Fig. 16. | Calculated array scalability of different types of two terminal nonvolatile memory. **(a-d)** Read margin versus crossbar array size (N) of the RRAM[35–39] (a), FTJ[40–42] (b), Fe-Diode[43–45] (c), and PCRAM[46] (d), respectively, using $V_R/3$ read scheme.

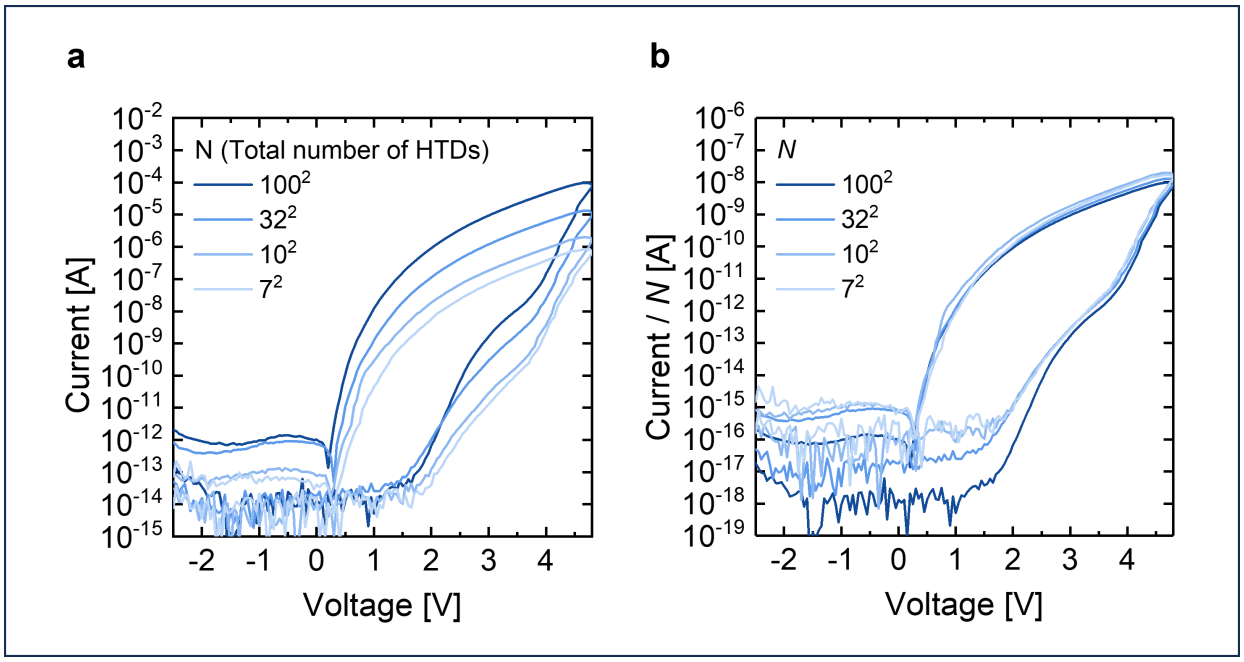

Supplementary Fig. 17. | Method to extract full DC I-V characteristics. (a,b) DC I-V characteristics of the 3D HTD are measured by aggregating the current contributions of multiple HTDs (a) and normalizing the current by the total number of devices (N) (b). The method assumes that the on-current remains constant regardless of the number of devices, enabling accurate extraction of the off-current as if from a single device.

Supplementary Text

Temperature-dependent conduction and switching mechanisms of FTJ and HTD We plotted ln(I/V^2) versus 1/V curves (F-N plot) in LRS to separate the current flow mechanisms of HTD and FTJ in Supplementary Fig. 6. According to the F-N tunneling current Equation S1, the slope of the extracted curves should be constant regardless of the temperature if F-N tunneling dominates the conduction mechanism[47].

$$I_{\mathrm{FN,T}} = \frac{q^3 A V^2}{8\pi t^2 h q \phi_{\mathrm{B}}} exp[\frac{-8\pi t (2q m_{\mathrm{T}}^*)^{\frac{1}{2}}}{3hV} \phi_{\mathrm{B}}^{\frac{3}{2}}] \tag{S1}$$

where q is the electronic charge, A is the dimension of devices, t is the dielectric thickness, h is Planck's constant, qϕ_{B} is the Schottky barrier height, and m_{T}^* is the tunneling effective mass in a dielectric. the slope of F-N plot of FTJ and HTD in polarization switching region is unchanged, regardless of the temperature (Supplementary Fig. 6c,e), which supports that the current conduction of FTJ is mainly determined by F-N tunneling.

Self-rectifying behavior of HTD In two-terminal tunnel junctions, the issue of sneak path problems poses a substantial threat to the scalability of crossbar arrays. Previous research efforts have adopted three-terminal Field-Effect Transistors (FETs) to address this challenge. However, the integration of FETs with tunnel junctions inevitably introduces complexities in fabrication and compromises scalability. Consequently, there is a need for the development of tunnel junctions endowed with rectification functionality, often referred to as self-rectifying junctions. The fabricated HTD exhibits exemplary rectifying characteristics attributed to the presence of an imprint field, also known as the built-in potential. It is widely acknowledged that one of the factors contributing to imprints is the presence of asymmetric interfacial layers, which stabilize a preferential polarization state. As corroborated by XPS analysis of the HTD (Supplementary Fig. 4), a significant degree of asymmetry exists between the top and bottom interfaces due to the inclusion of an oxygen scavenging layer (Ti) at the bottom electrode. This incorporation of Ti induces the generation of positively charged oxygen vacancies at the interface between HZO and Ti through

an oxidation-reduction process, resulting in a positive shift of the polarization-voltage hysteresis loop. Consequently, during a negative voltage sweep, the current is substantially attenuated, thereby manifesting intrinsic rectification properties. Moreover, due to the band alignment being mismatched between the top and bottom electrodes enhanced by oxygen vacancies, holes cannot tunnel into top electrode.

Comparison of FTJ and FeDiode Ferroelectric tunnel junctions (FTJs)[11,48] and ferroelectric diodes (FeDiodes)[43,49,50] share the basic structure of two-terminal ferroelectric memristors, typically comprising a metal-ferroelectric-metal (MFM) configuration. Both devices rely on the electroresistance effect, wherein the polarization state modulates the potential barrier between electrodes, controlling the current flow. However, few differences exist between FTJs and FeDiodes. Structurally, FTJs utilize an ultrathin ferroelectric (FE) layer (typically <5 nm), enabling direct quantum mechanical tunneling as the primary transport mechanism[51]. This direct tunneling yields distinct on and off states with exponential dependence on barrier height. In contrast, FeDiodes incorporate a thicker FE layer (>5 nm), which exceeds the direct tunneling limit, leading to dominant polarization-dependent leakage mechanisms, such as trap-assisted tunneling and Poole-Frenkel emission[43,45]. Regarding I-V characteristics, FTJs exhibit symmetrical switching driven primarily by polarization-induced modulation of the tunneling barrier, whereas FeDiodes display highly nonlinear and asymmetric diode-like rectifying behavior governed by interface Schottky barriers. Interestingly, our proposed HTD structurally resembles FeDiodes but exhibits a unique conduction mechanism wherein direct tunneling significantly contributes alongside defect-mediated tunneling. Furthermore, HTD switching characteristics depend not only on interface contact properties, such as Schottky barrier modulation but also on intrinsic bulk ferroelectric properties. Consequently, our HTD merges key attributes of both FTJs and FeDiodes, providing distinct insights into ferroelectric memristive device functionalities.

LFN spectroscopy for switching mechanism analysis Low-frequency noise (LFN) spectroscopy was utilized to delve into the diverse switching mechanisms observed in tunnel junctions. The $1/f$ noise behavior exhibited by FTJs can be elucidated through P-F emission, which is math-

ematically expressed as[52]:

$$\frac{S_{I_\mathrm{T}}}{I_\mathrm{T}^2} = \frac{\beta^2 N_D}{E\epsilon_{Si}^2 WL}\frac{q^2 A}{f} \tag{S2}$$

where β represents the fitting parameter, N_D denotes the trap density, E stands for the electric field, ϵ_{Si} signifies the permittivity of silicon, and A denotes the ratio of trap time constants. The FTJs exhibit $1/f$ noise behavior, with its magnitude escalating as V_{PGM} increases. When V_{PGM} is applied to metal, P_r induces an electric field with a bottom to top electrode direction in the HZO layer and a top to bottom electrode direction. As V_{PGM} rises, heightened P_r leads to a larger electric field in silicon, facilitating more electrons tunneling into the HZO layer. During the read operation, positive V_{READ} applied to metal induces an electric field in HZO that opposes the direction induced by P_r. Consequently, the electric field in HZO, governing P-F emission, diminishes with increasing V_{PGM}, thereby elevating S_{I_T} / I_T^2 (Equation S2). Unlike ferroelectric switching, S_{I_T} / I_T^2 of ionic memristor decreases with increasing V_{PGM}. This decrease in S_{I_T} / I_T^2 originates from phenomena like a reduction in the potential barrier height at the FE/DE interface due to the accumulation of oxygen vacancies with larger V_{PGM} applied to ionic memristors. Consequently, the potential barrier height diminishes at the interface, leading to a decrease in S_{I_T} / I_T^2. In this context, the LFN model is articulated as[53]:

$$\frac{S_{I_\mathrm{T}}}{I_\mathrm{T}^2} = \frac{4\alpha_H qL}{5A\epsilon\theta fV}\frac{q^2 A}{f} \tag{S3}$$

where q is the elementary charge, L is the distance between the contacts, ϵ is the dielectric constant, A is the cross-sectional area, θ is the ratio of free charge carriers to total charge carriers, and V is the applied voltage.

NLS model Domains exhibit uniform alignment along a specific direction when no electric fied is applied. Then, domains in ferroelectric film experience a change in their form hinge upon

the application of external electric field, including domain nucleation and subsequent growth of domain wall. Depending on the film qualities, there can be two switching mechanisms that can be explained by nucleation-limited switching (NLS) and Kolmogorov-Avrami-Ishibashi (KAI) switching models[54–57]. To quantify the kinetics of domain switching, we obtained a time-dependent switched polarization. We plotted the resulting data as a function of the pulse duration of FTJ and HTD (Extended Data Fig. 6a,b). In both cases, the results are well-fitted to the NLS model[54],

$$\Delta P(t) = 2P_S \int_{-\infty}^{\infty} [1 - exp(-\frac{t^n}{t_0})] \times F(logt_0) d(logt_0) \tag{S4}$$

where, P_{S} represents the spontaneous polarization, $F(logt_0)$ denotes a distribution function associated with the characteristic switching time, t_0. The parameter n represents the effective dimension of domain growth, with a value of 2 in this particular scenario. The expression within the square brackets in Equation S4 corresponds to the KAI switching model. Notably, this model does not account for spatial inhomogeneities in the film structure. In both FTJ and HTD, the NLS model fits the data (Extended Data Fig. 6a,b), demonstrating that the ferroelectric switching is determined by the nucleation of the domain.

Extraction of E_{N} and E_2 The polarization-switching process necessitates the nucleation of DWs aligned with the direction of the external E-field. Subsequently, these DWs expand and merge with each other, thereby completing the polarization switching. The expansion of DWs can be described by a thermally activated model overcoming an energy barrier. The hopping time (τ) required for this process is determined by the maximum energy barrier ($U_{\mathrm{B,max}}$) and T, which are represented as follows[55]

$$\tau \approx \tau_0 e^{\frac{U_{B,max}}{k_B T}} \tag{S5}$$

where k_{B} is the Boltzmann constant and τ_0 is a microscopic hopping time. Additionally,

$U_{\text{B,max}}$ varies with the external E-field and is expressed as follows[55]

$$U_{B,max} \approx U(1 - \frac{E}{E_{c0}})^{\gamma}(\frac{E_{c0}}{E})^{\mu} \tag{S6}$$

where U denotes the DW pinning energy or nucleation energy, E_{c0} represents the depinning threshold E at T = 0, μ is a dynamical exponent, and γ is a parameter related to the correlation between E and U. Consequently, according to Equation S6, as E increases, $U_{\text{B,max}}$ decreases, leading to a reduction in τ. When τ becomes smaller than $1/f$, the polarization switching is completed within the given pulse duration. This scenario is termed the 'DW expansion' region. When E is insufficient to complete DW formation during given pulse width, the ferroelectric switching does not occur. Combining Equations S5 and S6 and τ = $1/f$, the boundary condition (E_1) for the transition from relaxation to creep regime can be determined as follows[55]

$$\frac{E_1}{E_{c0}} \propto (\frac{U_{depin}}{k_B T})^{\frac{1}{\mu}}(1 - \frac{E_1}{E_{c0}})^{\frac{\gamma}{\mu}} \tag{S7}$$

where U_{depin} represents U at the boundary condition between relaxation and creep regimes, expressed as[55]

$$U_{depin} = U/lnln(\frac{1}{f_{\tau_0}}) \tag{S8}$$

Besides the creep regime, there exists another regime exhibiting a different E-f dependency. As E increases and U diminishes to a negligible level, the DW movement speed (v) shows a visco-flow characteristic that is linearly proportional to E ($v \propto E$). Thus, the following equation holds:

$$v \propto E\ exp\ exp[-(\frac{U}{k_B T})(\frac{E_{c0}}{E})^{\mu}(1 - \frac{E}{E_{c0}})^{\gamma}] \tag{S9}$$

Therefore, the boundary condition (E_2 = $E_c(f_{cr})$) for the transition from creep to flow regime is expressed as:

$$\frac{E_2}{E_{c0}} \propto (\frac{U}{k_B T})^{\frac{1}{\mu}} (1 - \frac{E_2}{E_{c0}})^{\frac{\gamma}{\mu}} \tag{S10}$$

Based on this, subsequent experiments observed changes in parameters such as E_1, E_2, and U_{depin}, in response to T variations in FTJ and HTD (Extended Data Fig. 6e). In order to confirm that E_2 accurately represents the transition from creep to flow regime, we compare the theoretical modeling results (line) with the actual measurements (scatter). The experimental data confirms the energies for nucleation (E_N) and transition from creep to flow regime (E_2), is decreased in HTD across all T ranges. These results can be explained by the oxygen vacancy factor.

DFT calculations To gain microscopic insights into the switching process, we performed density functional theory (DFT) calculations both in the presence and absence of oxygen vacancies (Fig. 2h). Our defective domain wall (DW) model[58], which incorporates V_O^{2+} species in the DW and adjacent bulk regions, yields DW energy of 263 mJ/m^2, which is substantially lower than that of the clean DW model. This result indicates that V_O^{2+} facilitates the DW formation. In contrast, the clean DW, without oxygen vacancies, exhibits a DW energy of 421 mJ/m^2 and a migration barrier of 0.237 eV per DW cell (Extended Data Fig. 6). Moreover, the initial formation of a DW inherently requires uniform polarization switching of several unit cells—a process that is accelerated by the presence of oxygen vacancies[59], particularly V_O^{2+}, thereby promoting the nucleation process (Supplementary Fig. 7 and 8). The acceleration of switching dynamics by V_Os can be attributed to the weakening of electrostatic repulsion between O ions; all the processes associated with polarization switching involve significant displacements of O ions to form a tetragonal-like atomic arrangement during the transition. Given that the atomic distances between neighboring O ions in the tetragonal-like structure are shorter than those in o-HfO_2, the repulsion between neighboring O ions should be a critical factor that interrupts the switching processes. In this context, the presence of V_Os can alleviate the difficulty in oxygen displacement. In particular, in V_O^{2+}, the

elimination of two extra electrons at the V_O site makes its impact even more significant than that of oxygen vacancies in other charge states (Supplementary Fig. 9 and 10), resulting in an energy barrier lowering for the ferroelectric switching.

Phase analysis in 3D HTD We successfully visualized the ferroelectric phase of HZO along the [010] zone axis, where the polarization of light oxygen atoms was clearly resolved. In HZO, ferroelectricity arises when the centrosymmetry of specific oxygen sites (O_{II}) is broken; this displacement from the ideal center causes electric polarization. Detecting subtle modulations in oxygen sites and the lattice symmetry differences among various polymorphs of HZO—including non-ferroelectric phases—has been challenging due to their similarity[60]. Using atomic resolution TEM imaging, particularly negative spherical aberration imaging (NCSI), which is well-suited for light element visualization, we characterized HZO as exhibiting a ferroelectric phase with space group $Pbc2_1$. Extended Data Fig. 7a shows a low-magnification image of the HZO thin film, while Extended Data Fig. 7b provides a magnified view where oxygen sites appear with bright contrast alongside Hf-Zr sites, indicating their lattice positions. Along the b-axis, displaced O_{II} sites are clearly visible, while O_I sites remain centered. The observed images consistently matched with the simulated images shown in Extended Data Fig. 7c, confirming the structural integrity of the ferroelectric HZO phase. Notably, Extended Data Fig. 7c shows grain aligned to the c-axis, corresponding to the polarization direction. While this alignment may enhance polarization in the device, it was not consistently observed across all grains, suggesting a limited impact. In addition to polar o-phase, HZO in 3D HTD also exhibit anti-polar phase ($Pbca$), as shown in Extended Data Fig. 7d.

Synaptic functionality of FTJ and HTD Long-term potentiation (LTP) and depression (LTD) characteristics are demonstrated by applying pulsed voltages (Extended Data Fig. 8b,c). In this work, we adopted an identical pulse scheme owing to its lower hardware and software costs compared with the incremental pulse method. In both devices, V_{PGM} (4 V, 1 ms) and erase pulse (V_{ERS}) (-2 V, 1ms) are applied to the top gate, while the bottom gate is grounded. Since the FTJ exhibits a very small dynamic range under this bias condition, we increased V_{PGM} to 5 V. Both the

FTJ and HTD exhibit 16-level conductance states and the FTJ and HTD show $g_{\max}/g_{\min}$ of 15.2 and 221.1, respectively, demonstrating the larger dynamic range of the HTD. Moreover, the HTD has a much smaller nonlinear factor (β) value in both LTP/LTD characteristics of 3.3 and 11.1 than those of the FTJ. Based on the synaptic functionality of on-chip learning, the Canadian Institute for Advanced Research (CIFAR-10) dataset was simulated using a nine-layer visual geometry group (VGG-9) network of convolutional neural networks (CNNs) (Extended Data Fig. 8a). The HTD achieves an image recognition accuracy of 89.2%, while the FTJ achieves 78.5% accuracy for the CIFAR-10 dataset after 100 epochs (Extended Data Fig. 8d), indicating that neuromorphic hardware for CNN can potentially utilize HTD with excellent synaptic characteristics.

Scalability of HTD To realize the inhibition of unselected cells during the read operation of the selected cell, various read bias schemes can be employed. In this work, we considered three representative schemes: float, V_{R}/2, V_{R}/3 schemes for evaluating the scalability of crossbar arrays with tunnel junctions (Supplementary Fig. 15). In the V_{R}/2 scheme, a voltage of V_{R}/2 is applied to all unselected lines. Under this configuration, cells that share the selected word and bit lines are biased at V_{R}/2, while all other cells connected to unselected lines remain at 0 V. The scalability of the crossbar array can be assessed numerically by considering the worst-case scenario during the read operation, wherein unselected cells are in the LRS. When a read voltage (V_{R}) is applied to the selected word line, a select current (I_{select}) traverses through the target cells, while an undesired sneak current (I_{sneak}) may flow through three unselected cells located in regions 1, 2, and 3 (Supplementary Fig. 15). This scenario is simplified to an equivalent circuit, depicted in Extended Data Fig. 9. The read margin (Δ V), normalized by the pull-up voltage (V_{pu}), is calculated utilizing the Kirchhoff equation, as delineated below:

$$\frac{\Delta V}{V_{pu}} = \frac{R_{pu}}{[R_{LRS}^{select} \| \frac{R_{LRS,1}^{sneak}}{N-1} + \frac{R_{LRS,2}^{sneak}}{(N-1)^2} + \frac{R_{LRS,3}^{sneak}}{N-1}] + R_{pu}} - \frac{R_{pu}}{[R_{HRS}^{select} \| \frac{R_{LRS,1}^{sneak}}{N-1} + \frac{R_{LRS,2}^{sneak}}{(N-1)^2} + \frac{R_{LRS,3}^{sneak}}{N-1}] + R_{pu}} \tag{S11}$$

where $R_{\mathrm{LRS}}^{select}$ and $R_{\mathrm{HRS}}^{select}$ are the resistance of the selected cell in the LRS and HRS, respec-

tively. $R^{sneak}_{\text{LRS,1}}$, $R^{sneak}_{\text{LRS,2}}$, and $R^{sneak}_{\text{LRS,3}}$ are the resistance of the unselected cells in regions 1, 2, and 3, respectively. R_{pu} is the pull-up resistance and N is the number of cells in the $N \times N$ crossbar array.

Based on equation S11, the scalability of the tunnel junctions are evaluated in each read scheme. In all read schemes, the crossbar array with HTD showcases significantly higher scalability than that with FTJ due to higher TER and rectifying ratios. The high TER and rectifying ratio facilitate the integration of approximately 10^7 cells within the array utilizing the HTD, representing a 10^4-fold improvement compared to the FTJ and demonstrating CMOS scalability previously unattainable. Supplementary Fig. 16 shows the extracted array scalability of two-terminal memristors, including RRAM[35–39], FTJ[40–42], Fe-Diode[43–45], and PCRAM[46], using this resistance model.

Extraction of accurate current density in 3D HTD Since the size of a single device of 3D HTD is small and the exact off current cannot be determined due to the limitation of the measurement resolution (B1500A), multiple devices were bundled and measured (Supplementary Fig. 17). When normalized by the number of elements, the same amount of current flowed. Therefore, the on/off ratio and rectification ratio were calculated based on the electrical characteristics of 10^4 devices. Based on this, the current density is obtained by dividing the area of the 3D HTD. Each layer—top electrode, ferroelectric layer, dielectric layer, and bottom electrode—has its own thickness and contributes individually to the total surface area of the HTD. Starting from the central hole, each layer wraps around the previous one, with the thickness of each layer adding to the overall radius of the cylinder. This layered structure allows us to treat each layer as a concentric "ring" around the hole, each with a specific inner and outer circumference based on its thickness. For each cylindrical layer, we calculate the surface area by considering the height of the structure and the difference between the outer and inner circumferences of the layer. Finally, to get the total area of the HTD, we add the individual areas of all layers (top electrode, ferroelectric, dielectric, and bottom electrode). Each layer contributes a unique area, which collectively gives the full surface area of the 3D.

Current density benchmark in HTD In the case of FTJs, the conduction mechanism primarily relies on tunneling, which results in a proportional decrease in current as the device size is scaled down. This low on-current density of tunnel junctions poses a significant challenge for achieving high-speed operation, particularly in densely integrated memory arrays. We overcome this limitation by utilizing ferroelectric-ionic hybrid switching. If ferroelectric polarization were the sole contributor, the increase in polarization with voltage would eventually saturate, inherently limiting the achievable current density. However, even after the saturation of ferroelectric polarization, additional barrier modulation driven by oxygen vacancy migration further increases in current density, resulting in higher current densities compared to conventional FTJs or ionic RRAMs (Extended Data Fig. 10a). Moreover, the self-rectifying behavior and enhanced electrostatic effects of the 3D HTD minimize leakage current at 0 V, which is a critical factor for maintaining energy efficiency in large-scale crossbar arrays. This dual advantage of high current density and low leakage current underscores the superiority of the HTD in addressing the challenges faced by conventional memristors.

1. Cagli, C. *et al.* Experimental and theoretical study of electrode effects in HfO_2 based RRAM. In *2011 International Electron Devices Meeting*, 28–7 (IEEE, 2011).

2. Zhang, H. *et al.* Role of interfacial layer on complementary resistive switching in the TiN/HfO_2/TiN resistive memory device. *Applied Physics Letters* **105** (2014).

3. Lin, C.-Y. *et al.* Attaining resistive switching characteristics and selector properties by varying forming polarities in a single HfO_2-based RRAM device with a vanadium electrode. *Nanoscale* **9**, 8586–8590 (2017).

4. Sun, C. *et al.* Control the switching mode of Pt/HfO_2/TiN RRAM devices by tuning the crystalline state of TiN electrode. *Journal of Alloys and Compounds* **749**, 481–486 (2018).

5. Ku, B., Abbas, Y., Sokolov, A. S. & Choi, C. Interface engineering of ALD HfO_2-based RRAM with ar plasma treatment for reliable and uniform switching behaviors. *Journal of Alloys and Compounds* **735**, 1181–1188 (2018).

6. Zhang, R. *et al.* Role of oxygen vacancies at the TiO_2/HfO_2 interface in flexible oxide-based resistive switching memory. *Advanced Electronic Materials* **5**, 1800833 (2019).

7. Li, Y. *et al.* High-uniformity threshold switching HfO_2-based selectors with patterned Ag nanodots. *Advanced Science* **7**, 2002251 (2020).

8. Zhang, Y. *et al.* Evolution of the conductive filament system in HfO_2-based memristors observed by direct atomic-scale imaging. *Nature communications* **12**, 7232 (2021).

9. Roy, S. *et al.* Toward a reliable synaptic simulation using Al-doped HfO_2 RRAM. *ACS applied materials & interfaces* **12**, 10648–10656 (2020).

10. Zahari, F. *et al.* Trap-assisted memristive switching in HfO_2-based devices studied by in situ soft and hard X-ray photoelectron spectroscopy. *Advanced Electronic Materials* **9**, 2201226 (2023).

11. Chanthbouala, A. *et al.* Solid-state memories based on ferroelectric tunnel junctions. *Nature nanotechnology* **7**, 101–104 (2012).

12. Ambriz-Vargas, F. *et al.* A complementary metal oxide semiconductor process-compatible ferroelectric tunnel junction. *ACS applied materials & interfaces* **9**, 13262–13268 (2017).

13. Goh, Y. & Jeon, S. The effect of the bottom electrode on ferroelectric tunnel junctions based on CMOS-compatible HfO_2. *Nanotechnology* **29**, 335201 (2018).

14. Wu, T.-Y. *et al.* Sub-na low-current HZO ferroelectric tunnel junction for high-performance and accurate deep learning acceleration. In *2019 IEEE International Electron Devices Meeting (IEDM)*, 6–3 (IEEE, 2019).

15. Mikheev, V. *et al.* Ferroelectric second-order memristor. *ACS applied materials & interfaces* **11**, 32108–32114 (2019).

16. Ma, C. *et al.* Sub-nanosecond memristor based on ferroelectric tunnel junction. *Nature communications* **11**, 1439 (2020).

17. Sulzbach, M. C. *et al.* Blocking of conducting channels widens window for ferroelectric resistive switching in interface-engineered $Hf_{0.5}Zr_{0.5}O_2$ tunnel devices. *Advanced Functional Materials* **30**, 2002638 (2020).

18. Shekhawat, A. *et al.* Data retention and low voltage operation of Al_2O_3/$Hf_{0.5}Zr_{0.5}O_2$ based ferroelectric tunnel junctions. *Nanotechnology* **31**, 39LT01 (2020).

19. Cheema, S. S. *et al.* One nanometer HfO_2-based ferroelectric tunnel junctions on silicon. *Advanced Electronic Materials* **8**, 2100499 (2022).

20. Chu, Y.-H. *et al.* Ultra-thin $Hf_{0.5}Zr_{0.5}O_2$ ferroelectric tunnel junction with high current density. In *2021 International Symposium on VLSI Technology, Systems and Applications (VLSI-TSA)*, 1–2 (IEEE, 2021).

21. Du, X. *et al.* High-speed switching and giant electroresistance in an epitaxial $Hf_{0.5}Zr_{0.5}O_2$-based ferroelectric tunnel junction memristor. *ACS Applied Materials & Interfaces* **14**, 1355–1361 (2021).

22. Gao, Z. *et al.* Giant electroresistance in hafnia-based ferroelectric tunnel junctions via enhanced polarization. *Device* **1** (2023).

23. Park, Y., Park, W. & Kim, S. Enhancing ferroelectricity in $HfAlO_x$-based ferroelectric tunnel junctions: A comparative study of MFS and MFIS structures with ultrathin interfacial layers. *Ceramics International* **50**, 26849–26857 (2024).

24. Kim, J. *et al.* Impact of HfO_2 dielectric layer placement in $Hf_{0.5}Zr_{0.5}O_2$-based ferroelectric tunnel junctions for neuromorphic applications. *Advanced Materials Technologies* **9**, 2400050 (2024).

25. Chen, Y.-F., Hsu, L.-W., Hu, C.-W., Lai, G.-T. & Wu, Y.-H. Enhanced tunneling electroresistance ratio for ferroelectric tunnel junctions by engineering metal work function. *IEEE Electron Device Letters* **43**, 208–211 (2021).

26. Goh, Y. *et al.* Selector-less ferroelectric tunnel junctions by stress engineering and an imprinting effect for high-density cross-point synapse arrays. *ACS applied materials & interfaces* **13**, 59422–59430 (2021).

27. Lim, S. *et al.* Dual-mode operations of self-rectifying ferroelectric tunnel junction crosspoint array for high-density integration of IoT devices. *IEEE Journal of Solid-State Circuits* **58**, 1860–1870 (2023).

28. Max, B., Pešić, M., Slesazeck, S. & Mikolajick, T. Interplay between ferroelectric and resistive switching in doped crystalline HfO_2. *Journal of Applied Physics* **123** (2018).

29. Sulzbach, M. C. *et al.* Unraveling ferroelectric polarization and ionic contributions to electroresistance in epitaxial $Hf_{0.5}Zr_{0.5}O_2$ tunnel junctions. *Advanced Electronic Materials* **6**, 1900852 (2020).

30. Mikheev, V. *et al.* Memristor with a ferroelectric HfO_2 layer: in which case it is a ferroelectric tunnel junction. *Nanotechnology* **31**, 215205 (2020).

31. Nukala, P. *et al.* Reversible oxygen migration and phase transitions in hafnia-based ferroelectric devices. *Science* **372**, 630–635 (2021).

32. Kang, S. *et al.* Highly enhanced ferroelectricity in HfO_2-based ferroelectric thin film by light ion bombardment. *Science* **376**, 731–738 (2022).

33. Shin, W. *et al.* Unveiling resistance switching mechanisms in undoped HfO_x ferroelectric tunnel junction using low-frequency noise spectroscopy. *IEEE Electron Device Letters* **44**, 345–348 (2022).

34. Koo, R.-H. *et al.* Comparative analysis of n-and p-type ferroelectric tunnel junctions through understanding of non-FE resistance switching. *IEEE Electron Device Letters* **44**, 1624–1627 (2023).

35. Jeon, K. *et al.* Purely self-rectifying memristor-based passive crossbar array for artificial neural network accelerators. *Nature communications* **15**, 129 (2024).

36. Yoon, J. H. *et al.* $Pt/Ta_2O_5/HfO_{2-x}/Ti$ resistive switching memory competing with multilevel NAND flash. *Advanced Materials* **27**, 3811–3816 (2015).

37. Jang, Y. H. *et al.* Memristive crossbar array-based probabilistic graph modeling. *Advanced Materials* **36**, 2403904 (2024).

38. Wu, C. *et al.* Self-rectifying resistance switching memory based on a dynamic p–n junction. *Nanotechnology* **32**, 085203 (2020).

39. Ni, R. *et al.* Controlled majority-inverter graph logic with highly nonlinear, self-rectifying memristor. *IEEE Transactions on Electron Devices* **68**, 4897–4902 (2021).

40. Hwang, J. *et al.* Ultra-high tunneling electroresistance ratio ($2\times\ 10^4$) & endurance (10^8) in oxide semiconductor-hafnia self-rectifying ($1.5\times\ 10^3$) ferroelectric tunnel junction. In *2023 IEEE Symposium on VLSI Technology and Circuits (VLSI Technology and Circuits)*, 1–2 (IEEE, 2023).

41. Goh, Y. *et al.* High performance and self-rectifying hafnia-based ferroelectric tunnel junction for neuromorphic computing and TCAM applications. In *2021 IEEE International Electron Devices Meeting (IEDM)*, 17–2 (IEEE, 2021).

42. Lee, J.-Y. *et al.* 3D stackable vertical ferroelectric tunneling junction (V-FTJ) with on/off ratio 1500x, applicable cell current, self-rectifying ratio 1000x, robust endurance of 10^9 cycles, multilevel and demonstrated macro operation toward high-density BEOL NVMs. In *2023 IEEE symposium on VLSI technology and circuits (VLSI technology and circuits)*, 1–2 (IEEE, 2023).

43. Luo, Q. *et al.* A highly CMOS compatible hafnia-based ferroelectric diode. *Nature communications* **11**, 1391 (2020).

44. Bae, H. *et al.* Ferroelectric diodes with sub-ns and sub-fJ switching and its programmable network for logic-in-memory applications. In *2021 Symposium on VLSI Technology*, 1–2 (IEEE, 2021).

45. Sarkar, S. *et al.* Multistate ferroelectric diodes with high electroresistance based on van der Waals heterostructures. *Nano Letters* **24**, 13232–13237 (2024).

46. Shuang, Y. *et al.* Bidirectional selector utilizing hybrid diodes for PCRAM applications. *Scientific Reports* **9**, 20209 (2019).

47. Lenzlinger, M. & Snow, E. Fowler-Nordheim tunneling into thermally grown SiO_2. *Journal of Applied physics* **40**, 278–283 (1969).

48. Wen, Z., Li, C., Wu, D., Li, A. & Ming, N. Ferroelectric-field-effect-enhanced electroresistance in metal/ferroelectric/semiconductor tunnel junctions. *Nature materials* **12**, 617–621 (2013).

49. Choi, T., Lee, S., Choi, Y., Kiryukhin, V. & Cheong, S.-W. Switchable ferroelectric diode and photovoltaic effect in $BiFeO_3$. *Science* **324**, 63–66 (2009).

50. Liu, X. *et al.* Aluminum scandium nitride-based metal–ferroelectric–metal diode memory devices with high on/off ratios. *Applied Physics Letters* **118** (2021).

51. Garcia, V. & Bibes, M. Ferroelectric tunnel junctions for information storage and processing. *Nature communications* **5**, 4289 (2014).

52. Shin, W. *et al.* Comprehensive and accurate analysis of the working principle in ferroelectric tunnel junctions using low-frequency noise spectroscopy. *Nanoscale* **14**, 2177–2185 (2022).

53. Shin, W. *et al.* 1/f noise in synaptic ferroelectric tunnel junction: Impact on convolutional neural network. *Advanced Intelligent Systems* **5**, 2200377 (2023).

54. Buragohain, P. *et al.* Nanoscopic studies of domain structure dynamics in ferroelectric la: HfO_2 capacitors. *Applied Physics Letters* **112** (2018).

55. Lim, S. Y., Park, M. S., Kim, A. & Yang, S. M. Nonlinear domain wall velocity in ferroelectric Si-doped HfO_2 thin film capacitors. *Applied Physics Letters* **118** (2021).

56. Yang, S. M. *et al.* Ac dynamics of ferroelectric domains from an investigation of the frequency dependence of hysteresis loops. *Physical Review B—Condensed Matter and Materials Physics* **82**, 174125 (2010).

57. Chen, Y.-C., Hsiang, K.-Y., Tang, Y.-T., Lee, M.-H. & Su, P. NLS based modeling and characterization of switching dynamics for antiferroelectric/ferroelectric hafnium zirconium oxides. In *2021 IEEE International Electron Devices Meeting (IEDM)*, 15–4 (IEEE, 2021).

58. Zhou, Y. *et al.* The effects of oxygen vacancies on ferroelectric phase transition of HfO_2-based thin film from first-principle. *Computational Materials Science* **167**, 143–150 (2019).

59. He, R., Wu, H., Liu, S., Liu, H. & Zhong, Z. Ferroelectric structural transition in hafnium oxide induced by charged oxygen vacancies. *Physical Review B* **104**, L180102 (2021).

60. Cheng, Y. *et al.* Reversible transition between the polar and antipolar phases and its implications for wake-up and fatigue in HfO_2-based ferroelectric thin film. *Nature communications* **13**, 645 (2022).